Modeling Discontinuous Axisymmetric Active Optical Membranes

James W. Rogers Jr.*
U.S. Air Force Research Laboratory, Wright–Patterson Air Force Base, Ohio 45433
and
Gregory S. Agnes†
Air Force Institute of Technology, Wright–Patterson Air Force Base, Ohio 45433

An active optical membrane is modeled as a laminate of inflatable structural material and piezopolymer sheets. Etching the electrode surfaces of each layer allows for selective actuation areas, which can be used to control surface regions independently. The analytical solution to a simplified axisymmetric system is discussed. The method of integral multiple scales is applied to the axisymmetric active membrane model and is studied. Results for both static and dynamic formulations are presented and indicate such a laminate can effectively deflect an optical membrane.

Nomenclature

A	=	circumferential cross-sectional area
$[C]_{n \times n}$	=	system damping matrix
c_1, c_2	=	axial, transverse speed of sound
D	=	flexural ridigity
d_{31}, d_{32}, d_{3r}	=	piezoelectric constant
$\{d(t)\}_{n \times 1}, \{d_u(t)\}_{n \times 1},$	=	displacement vector
$\{d_v(t)\}_{n \times 1}$		
E	=	Young's modulus
EH	=	radial stiffness
$EH_{\epsilon r}$	=	radial stiffness prestrain component
$EH_{\epsilon \theta}$	=	hoop stiffness prestrain component
EZ	=	radial stiffness prestrain/ unsymmetric component
EZ_ϵ	=	hoop stiffness prestrain/ unsymmetric component
g	=	independent variable
H	=	total laminate thickness
$K(\theta)$	=	torsional edge spring (can vary with θ)
$[K]_{n \times n}$	=	system mass matrix
$\mathbb{L}$	=	Lagrangian
$[M]_{n \times n}$	=	system mass matrix
N_i	=	initial axial load
N_r	=	radial tension
N_{rz}	=	tension component due to unsymmetric laminate
$N_{r\theta}$	=	cross tension component
N_θ	=	hoop tension
$\{N(x)\}_{1 \times n}, \{N_u(x)\}_{1 \times n},$	=	shape function vector
$\{N_v(x)\}_{1 \times n}$		
q	=	order
R	=	circular membrane radius
r, θ, z	=	cylindrical reference axes
$\mathbb{T}$	=	kinetic energy
T_n	=	timescales
t	=	time
U, Z	=	continuous Zernike modes
u, v, w	=	displacements
V	=	applied voltage
$\mathcal{V}$	=	integration volume
$\mathbb{V}$	=	potential energy
$\bar{V}$	=	discrete Zernike mode
y	=	maximum power
$\bar{\alpha}$	=	thermal constant
$\{\Gamma\}_{n \times 1}$	=	system forcing vector
δ	=	detuning parameter
ϵ	=	elastic strain
ϵ_0	=	prestrain
η, ξ, ζ	=	spatial scales
$\bar{\eta}^2$	=	speed ratio
ν	=	Poisson's ratio
ν_i, λ_i	=	eigenvector/eigenvalue pair
$\bar{\nu}$	=	variance
ρ	=	beam material density
σ	=	stress
σ_0	=	prestress
Ω	=	center frequency

Subscripts

q	=	order notation
$, g$	=	derivative with respect to variable g

Superscripts

c	=	composite asymptotic solution
T	=	transpose
$\hat{}$	=	dimensional value

*Aeronautical Engineer, Air Vehicles Directorate; james.rogers2@wpafb.af.mil. Member AIAA.

†Assistant Professor, Aeronautical and Astronautical Engineering Department; gregory.agnes@afit.edu. Senior Member AIAA.

Introduction

INFLATABLE space structures are the focus of current research due to launch volume and weight constraints. The inherent compliance of such materials, however, appears to limit the precision such a structure can maintain. A reflector's allowable error can be related to the wavelength of the energy being reflected. An optical reflector, assuming state-of-the-art adaptive optics techniques are implemented, requires a surface precision on the order of micrometers (Ref. 1). Couple this surface precision requirement to the large reflective area ($\sim 100 \text{ m}^2$) and the extremely thin, flexible structural material ($\sim 100 \ \mu\text{m}$), the modeling of this system proves challenging.

Current modeling techniques applied to inflatable reflectors include analytical and finite element approaches.[2] Analytical methods

provide great insight into the behavior of the system but quickly break down when a system of realistic complexity is examined. Approximation methods, such as finite elements, provide reasonable solutions for complex systems beyond the capabilities of analytical methods. Finite element methods, when applied to inflatable structures, tend to be troublesome due to the large-scale differences and structural compliances involved. When applied to optical reflectors, these methods are pushed beyond their limits. To counter these problems, very dense grids involving a large numbers of degrees of freedom are required. An approximation method with the flexibility of finite elements, but without the overhead resulting from its application to inflatables, is needed.

This paper is the fourth in a series introducing a new methodology that may be useful in the analysis of weakly nonlinear discontinuous systems. The first two papers presented the analytical development of a laminated piezoelectric membrane model. The analytical development, however, was limited to continuous systems. The third paper introduced the method of integral multiple scales (MIMS) as a method to model discontinuous dynamic systems with extreme high precision.[3-5]

This method, when used in a finite element formulation, provides an improved approximation method for analysis of inflatable optical reflectors. The necessary elements of the analytical solution of the selected problem are recalled, and MIMS is applied herein to an axisymmetric, two-dimensional, piezothermoelastic, laminated-plate model representing an axisymmetric active optical membrane.

Note that the notation used in this paper was required to condense the extremely large mathematical presentation without loss of detail. The notation, in general, follows the rule

$$M_{,xy} = \frac{\partial^2 M}{\partial x \partial y} \tag{1}$$

where M is the dependent variable or function and the variables following the comma in the subscript indicates partial differentiation. Additionally, asymptotic expansions are similarly expressed as

$$M_{i,xy} = \frac{\partial^2 M_i}{\partial x \partial y} \tag{2}$$

where the numeric value before the comma in the subscript indicates the asymptotic order of the dependent variable or function, for example, $M_2 \sim \mathcal{O}(\varepsilon^2)$. Also, the order of operations of the subscript notation is before the exponential operator as

$$M_{i,xy}^2 = \left(\frac{\partial^2 M_i}{\partial x \partial y} \right)^2 \tag{3}$$

Laminated Piezothermoelastic Plate Membrane

Beam-string is accepted nomenclature for a beam model that has such low bending stiffness that bending due to localized forcing results in localized curvature due to the high compliance of the system being modeled. Similarly, a very thin membranelike system can be modeled as a plate-membrane, where low bending stiffness results in localized effects. To develop the necessary fundamental equations used in this two-dimensional analysis, a system Lagrangian is needed.

Potential Energy

The potential energy of an elastic, circular plate (radius $= R$), with a torsional edge spring can be defined using the strain energy representation[6]

$$\hat{\mathbb{V}} = \int_{\hat{\mathcal{V}}} \left[\frac{1}{2} \{\hat{\epsilon}\}^T \{\hat{\sigma}\} - \{\hat{\epsilon}\}^T \{\hat{\sigma}_0\} + \{\hat{\epsilon}_0\}^T \{\hat{\sigma}\} \right] d\hat{\mathcal{V}} + \frac{1}{2} \hat{K}(\hat{\theta}) \hat{w}_{,\hat{r}}(R, \hat{t})^2 \tag{4}$$

with

$$\hat{\epsilon}_0 = \begin{pmatrix} \hat{\epsilon}_{0r} \\ \hat{\epsilon}_{0\hat{\theta}} \\ \hat{\epsilon}_{0r\hat{\theta}} \end{pmatrix} = \begin{pmatrix} \hat{\alpha}_r \\ \hat{\alpha}_\theta \\ 0 \end{pmatrix} T + \begin{pmatrix} \hat{d}_{31} \\ \hat{d}_{32} \\ 0 \end{pmatrix} \frac{\hat{V}}{t^*}$$

$$\hat{\sigma}_0 = \begin{pmatrix} \hat{\sigma}_{0r} \\ \hat{\sigma}_{0\hat{\theta}} \\ \hat{\sigma}_{0r\hat{\theta}} \end{pmatrix} = \begin{pmatrix} 1 \\ 0 \\ 0 \end{pmatrix} \frac{\hat{N}_i}{\hat{A}}$$

$$\hat{\sigma} = [\hat{E}]\{\hat{\epsilon}\} \tag{5}$$

where the material's modulus matrix $[E]$ in a state of plane stress can be represented as

$$[\hat{E}] = \frac{\hat{E}}{1 - \hat{v}^2} \begin{bmatrix} 1 & \hat{v} & 0 \\ \hat{v} & 1 & 0 \\ 0 & 0 & \frac{1}{2}(1 - \hat{v}) \end{bmatrix} \tag{6}$$

The addition of a torsional spring constant $\hat{K}(\hat{\theta})$ at the edge of the plate allows for variable boundary conditions. The caret is used throughout to indicate the variable is considered a dimensional value (prenormalization).

If we consider the radial, tangential, and transverse deflections of a thin, circular plate are represented as $\hat{u}$, $\hat{v}$ and $\hat{w}$, respectively, the general strain formula[7] in a cylindrical coordinate frame of the neutral plane in the state of plane stress, neglecting in-plane quadratic terms, is

$$\hat{\epsilon} = \begin{pmatrix} \hat{\epsilon}_{\hat{r}\hat{r}} \\ \hat{\epsilon}_{\hat{\theta}\hat{\theta}} \\ \hat{\epsilon}_{\hat{r}\hat{\theta}} \end{pmatrix} = \begin{pmatrix} \hat{u}_{,\hat{r}} + \frac{1}{2}\hat{w}_{,\hat{r}}^2 \\ \frac{\hat{u}}{\hat{r}} + \frac{1}{\hat{r}}\hat{v}_{,\hat{\theta}} + \frac{1}{2}\frac{1}{\hat{r}^2}\hat{w}_{,\hat{\theta}}^2 \\ \frac{1}{\hat{r}}\hat{u}_{,\hat{\theta}} + \hat{v}_{,\hat{r}} - \frac{\hat{v}}{\hat{r}} + \frac{1}{\hat{r}}\hat{w}_{,\hat{\theta}}\hat{w}_{,\hat{r}} \end{pmatrix} \tag{7}$$

where, if we assume through-the-thickness shear is linear during deformation, a representation of the strain field through the laminate can then be derived as

$$\hat{\epsilon} = \begin{pmatrix} \hat{u}_{,\hat{r}} + \frac{1}{2}\hat{w}_{,\hat{r}}^2 - \hat{z}\hat{w}_{,\hat{r}\hat{r}} \\ \frac{\hat{u}}{\hat{r}} + \frac{1}{\hat{r}}\hat{v}_{,\hat{\theta}} + \frac{1}{2}\frac{1}{\hat{r}^2}\hat{w}_{,\hat{\theta}}^2 - \hat{z}\left[\frac{1}{\hat{r}^2}\hat{w}_{,\hat{\theta}\hat{\theta}} + \frac{1}{\hat{r}}\hat{w}_{,\hat{r}} \right] \\ \frac{1}{\hat{r}}\hat{u}_{,\hat{\theta}} + \hat{v}_{,\hat{r}} - \frac{\hat{v}}{\hat{r}} + \frac{1}{\hat{r}}\hat{w}_{,\hat{\theta}}\hat{w}_{,\hat{r}} - 2\hat{z}\left[\frac{1}{\hat{r}}\hat{w}_{,\hat{r}\hat{\theta}} - \frac{1}{\hat{r}^2}\hat{w}_{,\hat{\theta}} \right] \end{pmatrix} \tag{8}$$

When Eq. (8) is applied to Eq. (4), the system's potential energy can be derived:

$$\hat{\mathbb{V}} = \int_{\hat{\mathcal{V}}} \left\{ \frac{E}{2(1 - v^2)} \left[\hat{\epsilon}_{\hat{r}\hat{r}}^2 + 2\hat{\epsilon}_{\hat{r}\hat{r}}\hat{\epsilon}_{\hat{\theta}\hat{\theta}} + \hat{\epsilon}_{\hat{\theta}\hat{\theta}}^2 + (1 - v)\hat{\gamma}_{\hat{r}\hat{\theta}}^2 \right] \right.$$

$$\left. + \hat{\sigma}_{0\hat{r}}\hat{\epsilon}_{\hat{r}\hat{r}} + \hat{\sigma}_{0\hat{\theta}}\hat{\epsilon}_{\hat{\theta}\hat{\theta}} + \hat{\sigma}_{0\hat{r}\hat{\theta}}\hat{\gamma}_{\hat{r}\hat{\theta}} \right\} d\hat{\mathcal{V}} + \frac{1}{2}\hat{K}(\hat{\theta})\hat{w}_{,\hat{r}}(R, \hat{t})^2 \tag{9}$$

To clarify, here $\hat{u}$, $\hat{v}$, and $\hat{w}$ are the displacements measured in the $\hat{r}$, $\hat{\theta}$, and $\hat{z}$ coordinate frame.

Kinetic Energy

When rotatory inertia is neglected, the plate's kinetic energy can be represented as

$$\hat{\mathbb{T}} = \frac{1}{2}\int_{\hat{\mathcal{V}}} \hat{\rho}\left(\hat{u}_{,\hat{t}}^2 + \hat{v}_{,\hat{t}}^2 + \hat{w}_{,\hat{t}}^2 \right) d\hat{\mathcal{V}} \tag{10}$$

Lagrangian

Equations (4–10) can now be used here to derive the unscaled system Lagrangian of laminated piezothermoelastic plate membrane:

$$
\hat{\mathbb{L}} = \int_{\hat{\mathcal{V}}} \Bigg(\frac{1}{2}\hat{\rho}\big[\hat{u}_{,\hat{t}}^2 + \hat{v}_{,\hat{t}}^2 + \hat{w}_{,\hat{t}}^2\big]
$$

$$
- \frac{E}{1-\nu^2}\hat{\epsilon}_{0\hat{r}}\left\{\left(\hat{u}_{,\hat{r}} + \frac{1}{2}\hat{w}_{,\hat{r}}^2\right) + \nu\left[\frac{1}{\hat{r}}(\hat{u} + \hat{v}_{,\hat{\theta}}) + \frac{1}{2\hat{r}^2}\hat{w}_{,\hat{\theta}}^2\right]\right\}
$$

$$
+ \frac{E\hat{z}}{1-\nu^2}\hat{\epsilon}_{0\hat{r}}\left[\frac{1}{2}\hat{w}_{,\hat{r}\hat{r}} + \nu\left(\frac{1}{\hat{r}}\hat{w}_{,\hat{r}} + \frac{1}{\hat{r}^2}\hat{w}_{,\hat{\theta}\hat{\theta}}\right)\right]
$$

$$
- \frac{E}{1-\nu^2}\hat{\epsilon}_{0\hat{\theta}}\left\{\left[\frac{1}{\hat{r}}(\hat{u} + \hat{v}_{,\hat{\theta}}) + \frac{1}{2\hat{r}^2}\hat{w}_{,\hat{\theta}}^2\right] + \nu\left(\hat{u}_{,\hat{r}} + \frac{1}{2}\hat{w}_{,\hat{r}}^2\right)\right\}
$$

$$
+ \frac{E\hat{z}}{1-\nu^2}\hat{\epsilon}_{0\hat{\theta}}\left[\left(\frac{1}{\hat{r}}\hat{w}_{,\hat{r}} + \frac{1}{\hat{r}^2}\hat{w}_{,\hat{\theta}\hat{\theta}}\right) + \nu\frac{1}{2}\hat{w}_{,\hat{r}\hat{r}}\right]
$$

$$
- \frac{E}{2(1+\nu)}\epsilon_{0\hat{z}}\left[\frac{1}{\hat{r}}(\hat{u}_{,\hat{\theta}} - \hat{v} + \hat{w}_{,\hat{r}}\hat{w}_{,\hat{\theta}}) + \hat{v}_{,\hat{r}}\right]
$$

$$
+ \frac{E\hat{z}}{1+\nu}\hat{\epsilon}_{0\hat{z}}\left(\frac{1}{\hat{r}}\hat{w}_{,\hat{\theta}} - \frac{1}{\hat{r}^2}\hat{w}_{,\hat{r}\theta}\right)
$$

$$
- \frac{E}{2(1+\nu)}\left[\frac{1}{\hat{r}}(\hat{v} - \hat{u}_{,\hat{\theta}} - \hat{w}_{,\hat{r}}\hat{w}_{,\hat{\theta}} + 2\hat{z}\hat{w}_{,\hat{r}\hat{\theta}}) - \hat{v}_{,\hat{r}} - \frac{2\hat{z}}{\hat{r}^2}\hat{w}_{,\hat{\theta}}\right]^2
$$

$$
- \frac{1}{2}\frac{E}{1-\nu^2}\left(\hat{u}_{,\hat{r}} + \frac{1}{2}\hat{w}_{,\hat{r}}^2 - \hat{z}\hat{w}_{,\hat{r}\hat{r}}\right)^2
$$

$$
+ \frac{\nu E}{(1-\nu^2)}\left[\frac{1}{\hat{r}}\left(\hat{u} + \hat{v}_{,\hat{\theta}} + \frac{1}{2}\hat{w}_{,\hat{\theta}}^2\right)\right.
$$

$$
\left. - \hat{z}\left(\frac{1}{\hat{r}}\hat{w}_{,\hat{r}} + \frac{1}{\hat{r}^2}\hat{w}_{,\hat{\theta}\hat{\theta}}\right)\right]\left(\hat{u}_{,\hat{r}} + \frac{1}{2}\hat{w}_{,\hat{r}}^2 - \hat{z}\hat{w}_{,\hat{r}\hat{r}}\right)
$$

$$
+ \frac{N_{0\hat{r}}}{\hat{H}}\left(\hat{u}_{,\hat{r}} + \frac{1}{2}\hat{w}_{,\hat{r}}^2 - \hat{z}\hat{w}_{,\hat{r}\hat{r}}\right)
$$

$$
+ \frac{N_{\hat{r}\hat{\theta}}}{\hat{H}}\left[\hat{v}_{,\hat{r}} + \frac{1}{\hat{r}}(\hat{u}_{,\hat{\theta}} - \hat{v} + \hat{w}_{,\hat{r}}\hat{w}_{,\hat{\theta}}) + 2\hat{z}\left(\frac{1}{\hat{r}^2}\hat{w}_{,\hat{\theta}} - \frac{1}{\hat{r}}\hat{w}_{,\hat{r}\theta}\right)\right]
$$

$$
\times \frac{N_{0\hat{\theta}}}{\hat{H}}\left[\frac{1}{\hat{r}}(\hat{u} + \hat{v}_{,\hat{\theta}}) + \frac{1}{2\hat{r}^2}\hat{w}_{,\hat{\theta}}^2 - \hat{z}\left(\frac{1}{\hat{r}}\hat{w}_{,\hat{r}} + \frac{1}{\hat{r}^2}\hat{w}_{,\hat{\theta}\hat{\theta}}\right)\right]\Bigg)\,d\hat{\mathcal{V}}
$$

$$
- \frac{1}{2}\hat{K}(\hat{\theta})\hat{w}_{,\hat{r}}(R,\hat{t})^2 \tag{11}
$$

Integrate through the thickness using

$$
\hat{\rho}\hat{H} = \int_{\hat{z}}\rho\,d\hat{z}, \qquad \hat{N}_{\hat{r}\hat{z}} = \int_{\hat{z}}\hat{\sigma}_{0\hat{r}}(A)\hat{z}\,d\hat{z}
$$

$$
\widehat{EH} = \int_{\hat{z}}\frac{E}{1-\nu^2}\,d\hat{z}, \qquad \hat{N}_{\hat{r}} = \int_{\hat{z}}\hat{\sigma}_{0\hat{r}}(A)\,d\hat{z}
$$

$$
\hat{N}_{\hat{\theta}} = \int_{\hat{z}}\hat{\sigma}_{0\hat{\theta}}(A)\,d\hat{z}, \qquad \hat{N}_{\hat{r}\hat{\theta}} = \int_{\hat{z}}\hat{\sigma}_{\hat{r}\hat{\theta}}(A)\,d\hat{z}
$$

$$
\widehat{EH}_{\hat{\epsilon}\hat{r}} = \int_{\hat{z}}\frac{E}{1-\nu^2}\hat{\epsilon}_{0\hat{r}}\,d\hat{z}, \qquad \widehat{EH}_{\hat{\epsilon}\hat{\theta}} = \int_{\hat{z}}\frac{E}{1-\nu^2}\hat{\epsilon}_{0\hat{\theta}}\,d\hat{z}
$$

$$
\widehat{EZ} = \int_{\hat{z}}\frac{E}{1-\nu^2}\hat{z}\,d\hat{z}, \qquad \widehat{EZ}_{\hat{\epsilon}} = \int_{\hat{z}}\frac{E}{1-\nu^2}\hat{\epsilon}_{0\hat{r}}\hat{z}\,d\hat{z}
$$

$$
\hat{D} = \int_{\hat{z}}\frac{E}{1-\nu^2}\hat{z}^2\,d\hat{z} \tag{12}
$$

The three-dimensional plate is effectively collapsed to a two-dimensional system. Note that, if the laminate is symmetric and all measurements are with respect to the neutral axis, then $\hat{N}_{\hat{r}\hat{z}} = 0$.

Analytical Solution

An analytical solution is possible for a continuous axisymmetric membrane. The results are presented in detail by Rogers and Agnes[8] and are summarized here. Each layer can have independent elastic, thermal, and piezoelectric properties. Again, elastically isotropic materials in each layer are assumed. When axisymmetry is assumed in loading, boundary conditions, etc., the system can be collapsed into a one-dimensional system.

As a result of the material properties concerned and the scaling choices used, it was shown that the in-plane equations decouple from the transverse equations through the first few asymptotic levels. Therefore, only the transverse system was discussed. When dynamic behavior was neglected, the system was solved using a two-level matching scheme resulting in the following composite solution to $\mathcal{O}(\varepsilon^4)$:

$$
w^c(r) = \varepsilon^2\frac{P_2}{4}(1-r^2) + \varepsilon^3\left[\frac{K}{K-1}\left(\frac{P_2}{2} + \frac{EZ_{\epsilon3}}{K}\right)(e^{-\xi} - 1)\right]
$$

$$
+ \varepsilon^4\left[\frac{P_2}{4}\bar{\eta}^2(1+\nu)EH_{\epsilon2}(1-r^2)\right]
$$

$$
+ \varepsilon^4\left\{\frac{K}{K-1}\left[\frac{2K-3+2\nu}{K-1}\left(\frac{P_2}{2} + \frac{EZ_{\epsilon3}}{K}\right)\right.\right.
$$

$$
\left.\left. - \frac{EZ_{\epsilon3}}{K^2}\right](e^{-\xi} - 1)\right\} \tag{13}
$$

where

$$
\xi = (1-r)/\varepsilon \tag{14}
$$

The numeric subscripts represent notational elements indicating the term's order relative to the parameter ε.

Figure 1 shows the transverse deflection of a piezoelectric laminate plate membrane with a pressure differential and axisymmetric edge conditions. This laminate has a 15 cm diameter, simple two-layer construction with a layer of Kapton® and a layer of polyvinylidine fluoride (PVDF) with the properties listed in Table 1.

An actuation potential corresponding to $\hat{d}_{31}\hat{V} = -5 \times 10^{-10}$ m applied through prestrain [Eq. (5)] causes a significant deviation in the center portion of the plate accounting for several wavelengths of visible light. Optical metrology is often concerned with circular wave fronts. Because of the small deflections concerned in this analysis, advantageous use of techniques developed for wave front analysis will be used. Figures 2 and 3 show the change in the reflected wave front. Both Figs. 2 and 3 present the Zernike coefficients for modes less than 16. Zernike functions provide an excellent alternative for viewing actual surface shaping effects. The Appendix presents a short overview and graphic illustration of the Zernike functions.

Figure 2 indicates, as expected, the reflected wave front is dominated by the axisymmetric modes. Figure 3 is the change in the wave front due to actuation, which is axisymmetric because bidirectional material properties were assumed. The effective boundary-layer region is approximately $\mathcal{O}(\sqrt{\varepsilon})$, as expected from the original

Table 1 Material properties

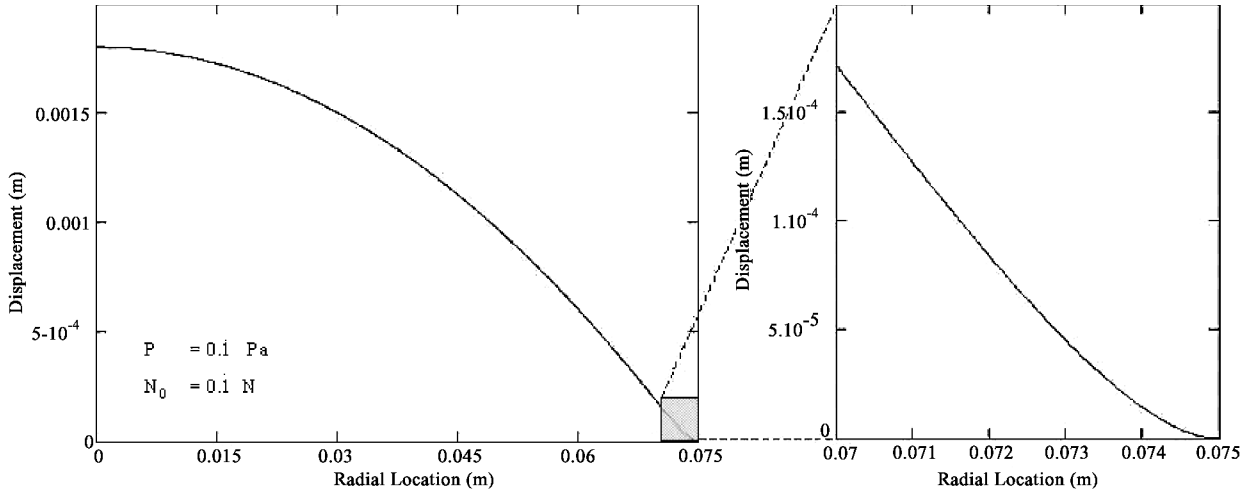| Property	Kapton	Bidirectional PVDF
Modulus E, GPa	2.8	1.8
Thickness H, μm	100	50
Poisson ratio ν	0.34	
CTE α, μm/m $\cdot$ °C	30	140
Density ρ, g/cm^3	1.42	1.79
Piezocoefficient d_{3i}, pC/N		−16

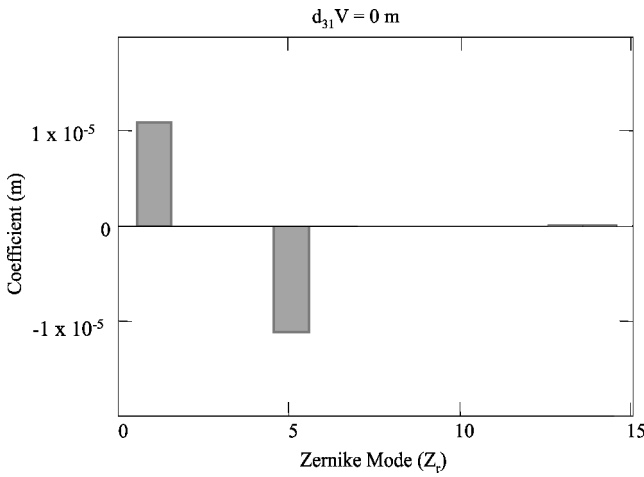**Fig. 1   Axisymmetric plate deflection (nondimensional).**

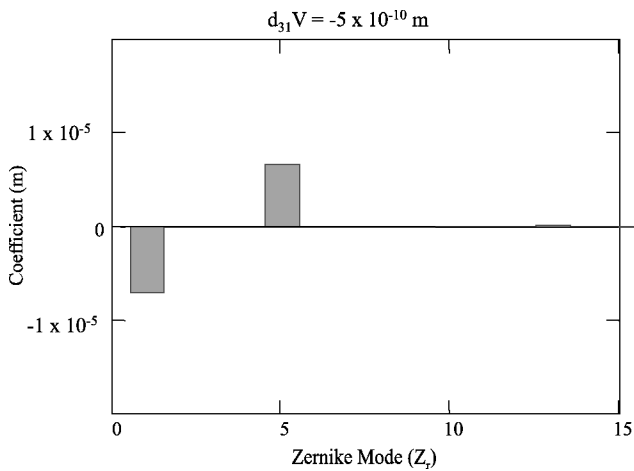**Fig. 2   Axisymmetric plate Zernike deviation.**

Fig. 3   Piezoelectric actuation effect.

mathematical foundation and is considered to have a small effect on the membrane away from this region.

This solution provides insight into the mechanical behavior of a membrane illustrating the localized curvatures inherent in such a compliant system. The analytic solution, however, is unable to model discontinuous properties throughout the membrane that would be present in an active membrane using spatially distributed electrode regions. A finite element method could provide effective modeling of the discrete system if the resulting precision was

adequate for optical applications. The MIMS introduced by Rogers to derive an asymptotic finite element model can satisfy these requirements.[5]

Finite Element Modeling

The analytical approach already discussed derives the equations of motion, non-dimensionalizes and scales them, then applies perturbation methods to yield a solution. When MIMS is used, an asymptotic system of finite element equations can be produced that can provide the desired solution.[5] When MIMS is used, the equations of motion derivation is bypassed to arrive at a solution that also allows for more complex analysis through the application of finite elements. To perform a perturbation analysis of this system properly, the Lagrangian must first be nondimensionalized. When axisymmetric properties are applied to Eq. (11) and the first-order pressure terms are inserted, the axisymmetric Lagrangian is formulated,

$$\hat{\mathbb{L}} = \int_{\hat{\mathcal{V}}} \left\{ \frac{1}{2}\hat{\rho}\left(\hat{u}_{,\hat{t}}^2 + \hat{v}_{,\hat{t}}^2 + \hat{w}_{,\hat{t}}^2\right) - \frac{E}{1-\nu^2}\hat{\epsilon}_{0\hat{\theta}}\left[\left(\hat{u}_{,\hat{r}} + \frac{1}{2}\hat{w}_{,\hat{r}}^2\right) + \nu\frac{1}{\hat{r}}\hat{u}\right] \right.$$

$$+ \frac{E\hat{z}}{1-\nu^2}\hat{\epsilon}_{0\hat{\theta}}\left(\hat{w}_{,\hat{r}\hat{r}} + \nu\frac{1}{\hat{r}}\hat{w}_{,\hat{r}}\right)$$

$$- \frac{E}{1-\nu^2}\hat{\epsilon}_{0\hat{r}}\left[\frac{1}{\hat{r}}\hat{u} + \nu\left(\hat{u}_{,\hat{r}} + \frac{1}{2}\hat{w}_{,\hat{r}}^2\right)\right]$$

$$+ \frac{E\hat{z}}{1-\nu^2}\hat{\epsilon}_{0\hat{r}}\left(\frac{1}{\hat{r}}w_{,\hat{r}} + \nu\hat{w}_{,\hat{r}\hat{r}}\right)$$

$$+ \frac{E}{1+\nu}\hat{\epsilon}_{0\hat{z}}\left(\frac{1}{\hat{r}}\hat{v} - \hat{v}_{,\hat{r}}\right) - \frac{E}{1+\nu}\left(\frac{1}{\hat{r}}\hat{v} - \hat{v}_{,\hat{r}}\right)^2$$

$$- \frac{1}{2}\frac{E}{1-\nu^2}\left\{\left(\hat{u}_{,\hat{r}} + \frac{1}{2}\hat{w}_{,\hat{r}}^2\right)\left[\left(\hat{u}_{,\hat{r}} + \frac{1}{2}\hat{w}_{,\hat{r}}^2\right) + \nu\frac{1}{\hat{r}}\hat{u}\right]\right\}$$

$$- \frac{1}{2}\frac{E}{1-\nu^2}\left\{\frac{1}{\hat{r}}\hat{u}\left[\frac{1}{\hat{r}}\hat{u} + \nu\left(\hat{u}_{,\hat{r}} + \frac{1}{2}\hat{w}_{,\hat{r}}^2\right)\right]\right\}$$

$$+ \frac{1}{2}\frac{E\hat{z}}{1-\nu^2}\left\{\hat{w}_{,\hat{r}\hat{r}}\left[\left(\hat{u}_{,\hat{r}} + \frac{1}{2}\hat{w}_{,\hat{r}}^2\right) + \nu\frac{1}{\hat{r}}\hat{u}\right]\right\}$$

$$+ \frac{1}{2}\frac{E\hat{z}}{1-\nu^2}\left[\left(\hat{u}_{,\hat{r}} + \frac{1}{2}\hat{w}_{,\hat{r}}^2\right)\left(\hat{w}_{,\hat{r}\hat{r}} + \nu\frac{1}{\hat{r}}\hat{w}_{,\hat{r}}\right)\right]$$

$$+ \frac{1}{2}\frac{E\hat{z}}{1-\nu^2}\left\{\frac{1}{\hat{r}}\hat{w}_{,\hat{r}}\left[\frac{1}{\hat{r}}\hat{u} + \nu\left(\hat{u}_{,\hat{r}} + \frac{1}{2}\hat{w}_{,\hat{r}}^2\right)\right]\right\}$$

$$+ \frac{1}{\hat{r}}\hat{u}\left(\frac{1}{\hat{r}}\hat{w}_{,\hat{r}} + \nu\hat{w}_{,\hat{r}\hat{r}}\right)\Bigg\}$$

$$- \frac{1}{2}\frac{E\hat{z}^2}{1-\nu^2}\left[\hat{w}_{,\hat{r}\hat{r}}\left(\hat{w}_{,\hat{r}\hat{r}} + \nu\frac{1}{\hat{r}}\hat{w}_{,\hat{r}}\right) + \frac{1}{\hat{r}}\hat{w}_{,\hat{r}}\left(\frac{1}{\hat{r}}w_{,\hat{r}} + \nu\hat{w}_{,\hat{r}\hat{r}}\right)\right]$$

$$+ \frac{N_{0\hat{r}}}{\hat{H}}\left(\hat{u}_{,\hat{r}} + \frac{1}{2}\hat{w}_{,\hat{r}}^2\right) - \frac{N_{\hat{r}\hat{z}}}{\hat{H}}\hat{w}_{,\hat{r}\hat{r}} + \frac{N_{0\hat{\theta}}}{\hat{H}}\frac{1}{\hat{r}}\hat{u} - \frac{N_{\hat{\theta}\hat{z}}}{\hat{H}}\frac{1}{\hat{r}}\hat{w}_{,\hat{r}}\Bigg\}\,\mathrm{d}\hat{\mathcal{V}}$$

$$+ \int_{\hat{r}}\hat{P}(\hat{w} + \hat{u}_{,\hat{r}}\hat{w} - \hat{w}_{,\hat{r}}\hat{u})\,\mathrm{d}\hat{r} - \frac{1}{2}\hat{K}(\hat{\theta})\hat{w}_{,\hat{r}}(R,\hat{t})^2 \qquad (15)$$

where

$$\hat{\epsilon}_{0\hat{r}} = \hat{\epsilon}_{0\hat{\theta}} = (d_{3r}V/t) + \bar{\alpha}T \qquad (16)$$

$$N_{0\hat{r}} = N_{0\hat{\theta}} \qquad (17)$$

$$N_{\hat{r}\hat{z}} = N_{\hat{\theta}\hat{z}} = 0 \qquad (18)$$

These parameters were chosen assuming symmetric edge loading and bidirectional thermoelectric properties.

To perform a perturbation analysis of this system properly, the system must be put in nondimensional form. The following nondimensional parameter scaling rules are used:

$$r = \hat{r}/R, \qquad z = (\hat{z}/R)\bar{\eta}^2, \qquad u = (\hat{u}/R)\bar{\eta}^2$$

$$w = (\hat{w}/Rr^*)\bar{\eta}, \qquad v = (\hat{v}/R)\bar{\eta}^2, \qquad t^2 = \left(c_2^2/R^2\right)\hat{t}^2$$

$$r^{*2} = (D/R^2\widehat{EH})\bar{\eta}^2, \qquad \bar{\eta}^2 = c_1^2/c_2^2, \qquad N_r = 1/\bar{\eta}^2$$

$$N_{rz} = (\hat{N}_{\hat{r}\hat{z}}/REH)\bar{\eta}^2, \qquad N_\theta = N_r, \qquad N_r\theta = 0$$

$$EZ = (\widehat{EZ}/R\widehat{EH})\bar{\eta}^2, \qquad EZ_\epsilon = (\widehat{EZ}_{\hat{\epsilon}}/R\widehat{EH})\bar{\eta}^2$$

$$EH_{\epsilon r} = (\widehat{EH}_{\hat{\epsilon}\hat{r}}/\widehat{EH})\bar{\eta}^2, \qquad EH_{\epsilon\theta} = (\widehat{EH}_{\hat{\epsilon}\hat{\theta}}/\widehat{EH})\bar{\eta}^2$$

$$K(\theta) = [\hat{K}(\hat{\theta})/R\widehat{EH}]\bar{\eta}^2 \qquad (19)$$

where $c_1 = \sqrt{\widehat{EH}/\hat{\rho}\hat{H}}$ and $c_2 = \sqrt{\hat{N}_{\hat{r}}/\hat{\rho}\hat{H}}$ are the in-plane and transverse speeds of sound in the plate.

When Eqs. (12) and (19) are substituted into Eq. (15) and the spring edge conditions, that is $K(\theta) = 0$ are neglected, the scaled Lagrangian becomes

$$\mathbb{L} = \int_r \Bigg\{\frac{1}{2}\left[\frac{1}{\bar{\eta}^2}\left(u_{,t}^2 + v_{,t}^2\right) + w_{,t}^2\right]$$

$$- EH_{\epsilon z}\left(\frac{1}{r}v - v_{,r}\right) + EH_\epsilon\left[\left(u_{,r} + \frac{1}{r}u\right) + \frac{1}{2}w_{,r}^2\right]$$

$$- (1-\bar{v})\left(\frac{1}{r}v - v_{,r}\right)^2 - \hat{v}\left[\frac{1}{r}u\left(u_{,r} + \frac{1}{2}w_{,r}^2\right)\right]$$

$$- \frac{1}{2}\left(u_{,r}^2 + \frac{1}{r^2}u^2 + w_{,r}^2\right) - \left(\frac{1}{r}u + u_{,r} + \frac{1}{2}u_{,r}w_{,r}^2 - \frac{1}{8}w_{,r}^4\right)$$

$$- \frac{1}{2}\epsilon^2\left(w_{,rr}^2 + \frac{1}{r^2}w_{,r}^2\right) - D_{12}\left(\frac{1}{2}w_{,r}w_{,rr}\right)$$

$$+ EZ_{11}\left[w_{,rr}\left(u_{,r} + \frac{1}{2}w_{,r}^2\right) + \frac{1}{r^2}uw_{,r}\right]$$

$$+ EZ_{12}\left[\frac{1}{r}uw_{,rr} + \frac{1}{r}w_{,r}\left(u_{,r} + \frac{1}{2}w_{,r}^2\right)\right]$$

$$+ (N_z - EZ_\epsilon)\left(\frac{1}{r}w_{,r} + w_{,rr}\right) - P\left(w + \frac{1}{\eta}(u_{,r}w - w_{,r}u)\right)\Bigg\}\,\mathrm{d}r$$

$$(20)$$

where

$$EH_{\epsilon\theta} = EH_{\epsilon r}, \qquad EZ_{\epsilon\theta} = EZ_{\epsilon r}, \qquad EH_\epsilon = EH_{\epsilon 11} + EH_{\epsilon 12}$$

$$EZ_\epsilon = EZ_{\epsilon 11} + EZ_{\epsilon 12}, \qquad \bar{v} = EH_{12}/EH_{11} \qquad (21)$$

The boundary-layer areas are introduced through the stretching variables (or spatial scales):

$$u(r,t) \rightarrow u(\eta, \xi, \zeta, t; \varepsilon), \qquad v(r,t) \rightarrow v(\eta, \xi, \zeta, t; \varepsilon)$$

$$w(r,t) \rightarrow w(\eta, \xi, \zeta, t; \varepsilon) \qquad (22)$$

where $\eta = r$, $\xi = r/\varepsilon$, and $\zeta = (1-r)/\varepsilon$ are used to derive the analytical solution. When the chain rule is applied to $r = r(\eta, \xi, \zeta; \varepsilon)$, the differentials are transformed using

$$\frac{\mathrm{d}}{\mathrm{d}r} = \frac{\partial}{\partial\eta} + \frac{1}{\varepsilon}\left[\frac{\partial}{\partial\xi} - \frac{\partial}{\partial\zeta}\right] \qquad (23)$$

$$\frac{\mathrm{d}^2}{\mathrm{d}r^2} = \frac{\partial^2}{\partial\eta^2} + \frac{2}{\varepsilon}\left[\frac{\partial^2}{\partial\xi\,\partial\eta} - \frac{\partial^2}{\partial\zeta\,\partial\eta}\right] + \frac{1}{\varepsilon^2}\left[\frac{\partial^2}{\partial\xi^2} + \frac{\partial^2}{\partial\zeta^2} - 2\frac{\partial^2}{\partial\xi\,\partial\zeta}\right]$$

$$(24)$$

The resulting Lagrangian is now a multiple scales representation that includes the boundary region effects. In a continuous membrane, an analytical solution may be possible where the inner scale ξ should disappear leaving a solution similar to Eq. (13). The purpose of this analysis, however, is to produce a solution for a discontinuous membrane laminate. To develop a finite element representation, the independent variables can be replaced by the assumed shape function set and the unknown nodal displacements:

$$u(r,t) = \{N_u(r)\}\{d(t)\}, \qquad v(r,t) = \{N_v(r)\}\{d(t)\}$$

$$w(r,t) = \{N(r)\}\{d(t)\} \qquad (25)$$

Rogers[5] demonstrated the advantage of assuming shape function and displacement expansions at this level of the analysis, and that is done here also. Substituting the expansions (introducing temporal scaling)

$$t = \omega\tau \qquad (26)$$

$$T_n = \varepsilon^n\tau \qquad (27)$$

$$\omega = \omega_0 + \varepsilon\omega_1 + \varepsilon^2\omega_2 + \cdots \qquad (28)$$

$$N(\eta, \xi, \zeta; \varepsilon) = N_0(\eta, \xi, \zeta) + \varepsilon N_1(\eta, \xi, \zeta) + \cdots \qquad (29)$$

$$N_v(\eta, \xi, \zeta; \varepsilon) = N_{v0}(\eta, \xi, \zeta) + \varepsilon N_{v1}(\eta, \xi, \zeta) + \cdots \qquad (30)$$

$$N_u(\eta, \xi, \zeta; \varepsilon) = N_{u0}(\eta, \xi, \zeta) + \varepsilon N_{u1}(\eta, \xi, \zeta) + \cdots \qquad (31)$$

$$d(t; \varepsilon) = \varepsilon^2 d_2(t) + \varepsilon^3 d_3(t) + \varepsilon^4 d_4(t) + \cdots \qquad (32)$$

$$d_v(t; \varepsilon) = \varepsilon^3 d_{v3}(t) + \varepsilon^4 d_{v4}(t) + \varepsilon^5 d_{v5}(t) + \cdots \qquad (33)$$

$$d_u(t; \varepsilon) = \varepsilon^3 d_{u3}(t) + \varepsilon^4 d_{u4}(t) + \varepsilon^5 d_{u5}(t) + \cdots \qquad (34)$$

$$w(\eta, \xi, \zeta, t; \varepsilon) = N(\eta, \xi, \zeta; \varepsilon)d(t; \varepsilon) \qquad (35)$$

$$v(\eta, \xi, \zeta, t; \varepsilon) = N_v(\eta, \xi, \zeta; \varepsilon)d_v(t; \varepsilon) \qquad (36)$$

$$u(\eta, \xi, \zeta, t; \varepsilon) = N_u(\eta, \xi, \zeta; \varepsilon)d_u(t; \varepsilon) \qquad (37)$$

where $\omega_0 = 1$, because the original system was effectively scaled by $\hat{\omega}_0$, into Eq. (20) produces a multiple scales Lagrangian expansion. Separating the resulting expansion into ε-order groupings produces a Lagrangian expansion:

$$\mathbb{L} = \varepsilon^{-2}\mathbb{L}_{-2} + \varepsilon^{-1}\mathbb{L}_{-1} + \mathbb{L}_0 + \varepsilon\mathbb{L}_1 + \varepsilon^2\mathbb{L}_2 + \cdots \qquad (38)$$

Selecting the order of precision is equivalent to selecting an element in the energy expansion. Applying Euler's equations to the

selected Lagrangian element produces the system of finite element equations to produce the desired solution. The functions produced through the application of Euler's equations to $\mathbb{L}_n$ exists in the set of functions produced through the application of Euler's equations to $\mathbb{L}_m$, where $m > n$.

Similar to observations made in the analytical approach, the in-plane displacements are negligible to the order in this analysis, $\mathbb{L}_2$. Additionally, the axial displacements are not present in the transverse displacement equations at the level of expansion presented. Therefore, the in-plane displacements will not be considered in the remaining portion of this axisymmetric membrane analysis.

The system matrices can be calculated by applying either of the asymptotic shape functions previously presented.[5] The cubic C^1 shape function expansion is repeated here for clarity:

$$N^T = \begin{pmatrix} N_1 \\ N_2 \\ N_3 \\ N_4 \\ N_5 \\ N_6 \end{pmatrix} = \begin{pmatrix} 1 - 5\eta + 8\eta^2 - 4\eta^3 \\ 0 \\ \eta - 4\eta^2 + 4\eta^3 \\ 0 \\ 4\eta - 4\eta^2 \\ -2\eta + 6\eta^2 - 4\eta^3 \end{pmatrix}$$

$$+ \varepsilon \begin{pmatrix} 5 - 26\eta + 44\eta^2 - 24\eta^3 - 5e^{-\xi} + e^{-\zeta} \\ 1 - 5\eta + 8\eta^2 - 4\eta^3 - e^{-\xi} \\ -1 + 10\eta - 28\eta^2 + 24\eta^3 + e^{-\xi} - 5e^{-\zeta} \\ -\eta + 4\eta^2 - 4\eta^3 + e^{-\zeta} \\ -4 + 16\eta - 16\eta^2 + 4e^{-\xi} + 4e^{-\zeta} \\ 2 - 12\eta + 24\eta^2 - 16\eta^3 - 2e^{-\xi} + 2e^{-\zeta} \end{pmatrix}$$

$$+ \varepsilon^2 \begin{pmatrix} 26 - 140\eta + 248\eta^2 - 144\eta^3 - 26e^{-\xi} + 10e^{-\zeta} \\ 5 - 26\eta + 44\eta^2 - 24\eta^3 - 5e^{-\xi} + e^{-\zeta} \\ -10 + 76\eta - 184\eta^2 + 144\eta^3 + 10e^{-\xi} - 26e^{-\zeta} \\ 1 - 10\eta + 28\eta^2 - 24\eta^3 - e^{-\xi} + 5e^{-\zeta} \\ -16 + 64\eta - 64\eta^2 + 16e^{-\xi} + 16e^{-\zeta} \\ 12 - 72\eta + 144\eta^2 - 96\eta^3 - 12e^{-\xi} + 12e^{-\zeta} \end{pmatrix}$$

$$+ \varepsilon^3 \begin{pmatrix} 140 - 776\eta + 1424\eta^2 - 864\eta^3 - 140e^{-\xi} + 76e^{-\zeta} \\ 26 - 140\eta + 248\eta^2 - 144\eta^3 - 26e^{-\xi} + 10e^{-\zeta} \\ -76 + 520\eta - 1168\eta^2 + 864\eta^3 + 76e^{-\xi} - 140e^{-\zeta} \\ 10 - 76\eta + 184\eta^2 - 144\eta^3 - 10e^{-\xi} + 26e^{-\zeta} \\ -64 + 256\eta - 256\eta^2 + 64e^{-\xi} + 64e^{-\zeta} \\ 72 - 432\eta + 864\eta^2 - 576\eta^3 - 72e^{-\xi} + 72e^{-\zeta} \end{pmatrix}$$

$$+ \mathcal{O}(\varepsilon^4) \tag{39}$$

Figure 4 shows the behavior of these shape functions. These shape functions are as a result of selecting an ε value of 0.1. This value is extremely large but provides a better illustration of the boundary region effects.

When the cubic C^1 shape functions are applied and simplified, the resulting system, with modal damping terms added, is

$$M_0 d_{2,00} + K_0 d_2 = -\Gamma_0 \tag{40}$$

$$M_0 d_{3,00} + K_0 d_3 = -\Gamma_1 - (2\omega_1 M_0 + M_1)d_{2,00} + M_0 d_{2,01}$$

$$- K_1 d_2 - C_1 d_{2,0} \tag{41}$$

$$M_0 d_{4,00} + K_0 d_4 = -\Gamma_2 - (2\omega_1 M_0 + M_1)d_{3,00} + M_0 d_{3,01}$$

$$- K_1 d_3 - C_1 d_{3,0} - M_0 \big[d_{2,11} + 2d_{2,02} + 4\omega_1 d_{2,01}$$

$$+ \big(\omega_1^2 + 2\omega_2\big)d_{2,00} \big] - 2M_1(\omega_1 d_{2,00} + d_{2,01})$$

$$- M_2 d_{2,00} - K_2 d_2 - C_1 d_{2,1} - C_2 d_{2,0} \tag{42}$$
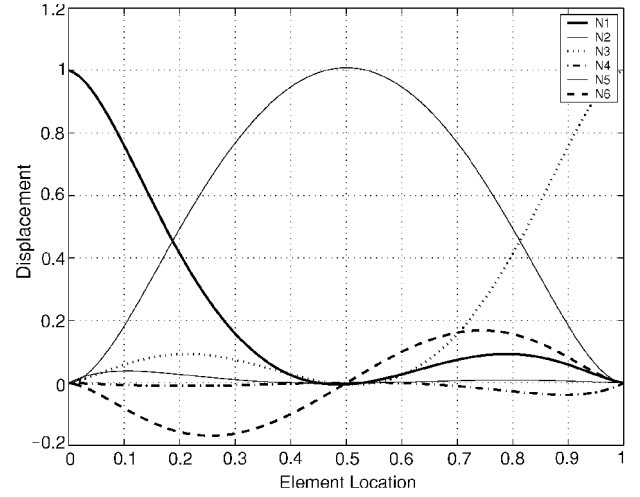

Fig. 4   Cubic C^1 shape functions, $\varepsilon = 0.1$.

The volumetric Lagrangian integral was reduced by integrating through the thickness to the following in cylindrical coordinates:

$$\int_A \mathrm{d}A = \int_A r\,\mathrm{d}\theta\,\mathrm{d}r \tag{43}$$

However, with axisymmetric assumptions, it becomes

$$\int_A \mathrm{d}A = 2\pi \int_r r\,\mathrm{d}r \tag{44}$$

which results in the following multiple scales integral:

$$\int_{r_1}^{r_2} f(r)r\,\mathrm{d}r$$

$$= \int_0^{(r_2 - r_1)/\varepsilon} \int_0^{(r_2 - r_1)/\varepsilon} \int_{r_1}^{r_2} f(\eta, \xi, \zeta; \varepsilon)\eta\,\mathrm{d}\eta\varepsilon\,\mathrm{d}\xi\varepsilon\,\mathrm{d}\zeta \tag{45}$$

For simplicity of notation, the following notation will be used to represent the multiple scales integral:

$$\int_{ms} f(\eta, \xi, \zeta; \varepsilon)\,\mathrm{d}_{ms}$$

$$= \int_0^{(r_2 - r_1)/\varepsilon} \int_0^{(r_2 - r_1)/\varepsilon} \int_{r_1}^{r_2} f(\eta, \xi, \zeta; \varepsilon)\eta\,\mathrm{d}\eta\varepsilon\,\mathrm{d}\xi\varepsilon\,\mathrm{d}\zeta \tag{46}$$

The system stiffness matrices can now be computed through the following:

$$K_0 = 2\pi \int_{ms} \big[G_1^T G_1 + F_1^T F_1 \big]\,\mathrm{d}_{ms} \tag{47}$$

$$K_1 = 2\pi \int_{ms} \big[G_1^T G_2 + G_2^T G_1 + F_1^T F_2 + F_2^T F_1 \big]$$

$$+ \frac{1}{\eta} D_{12} \big[G_1^T F_1 + F_1^T G_1 \big]\,\mathrm{d}_{ms} \tag{48}$$

$$K_2 = 2\pi \int_{ms} \big[G_2^T G_2 + G_1^T G_3 + G_3^T G_1 + F_2^T F_2 + F_1^T F_3 + F_3^T F_1 \big]$$

$$+ \frac{1}{\eta} D_{12} \big[G_1^T F_2 + F_2^T G_1 + F_1^T G_2 + G_2^T F_1 \big]$$

$$+ \frac{1}{\eta^2} \big[G_1^T G_1 \big] - E H_{\varepsilon 2} \big[G_1^T G_1 \big]\,\mathrm{d}_{ms} \tag{49}$$

where

$$F_i = [N_{i,\xi\xi} + N_{i,\zeta\zeta} - N_{i,\xi\zeta} + 2(N_{i-1,\zeta\eta} - N_{i-1,\xi\eta}) + N_{i-2,\eta\eta}]$$

$$G_i = [N_{i,\xi} - N_{i,\zeta}] + N_{i-1,\eta} \tag{50}$$

The system mass matrices are computed through

$$M_0 = 2\pi \int_{ms} \left[N_0^T N_0 \right] d_{ms} \quad (51)$$

$$M_1 = 2\pi \int_{ms} \left[N_0^T N_1 + N_1^T N_0 \right] d_{ms} \quad (52)$$

$$M_2 = 2\pi \int_{ms} \left[N_1^T N_1 + N_0^T N_2 + N_2^T N_0 \right] d_{ms} \quad (53)$$

The forcing vectors are similarly produced:

$$\Gamma_0 = 2\pi \int_{ms} -P N_0^T d_{ms}$$

$$\Gamma_1 = 2\pi \int_{ms} \left[(N_{z3} - E Z_{\epsilon3}) F_1^T - P N_1^T \right] d_{ms}$$

$$\Gamma_2 = 2\pi \int_{ms} \left[(N_{z3} - E Z_{\epsilon3}) \left(F_2^T + \frac{1}{\eta} G_1^T \right) - P N_2^T \right] d_{ms} \quad (54)$$

As seen in the analytical solution, the actuation manifests itself through an axial strain term $E H_{\epsilon2}$ and a boundary moment term $E Z_{\epsilon3}$, which are evident here. The axial term modifies the system stiffness, and the boundary term acts as an applied forcing term. This system can be used to analyze systems whose solutions are unattainable through analytical methods.

Results

Two piezoelastic laminated membrane patterns are considered and shown in Fig. 5 with the properties in Table 1. The first pattern consists of an electrode etching equally splitting the radius. The second pattern has three concentric electrode etchings of equal radial lengths. More etching patterns are obviously possible, but these can provide the necessary initial insight for more complicated design considerations. These patterns will indicate the effect of increasing the electrode area as well as providing concentric rings of potential surface allowing different potentials. Both shaping and dynamic response studies can be performed.

Shaping

The use of Zernike coefficients is a good mechanism to compare the effects of shape modifications. Because of the extremely small displacements present in the membranes modeled, a reflected wave front aberration can be approximated as twice the surface displacement. In the Appendix, the mapping method between wave front aberrations and Zernike coefficients is discussed.

Several configurations are presented in Table 2, where the sign indicates the relative voltage potential in each area. Figure 6 shows the result of the piezoelectric effects when configuration 0 is concerned. With a continuous electrode, this model can be compared to the analytical solution discussed earlier.
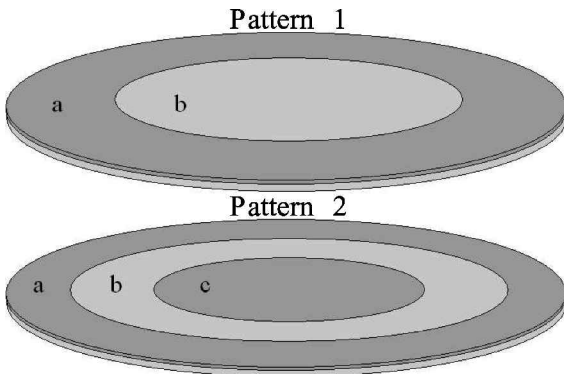

Fig. 5   Piezoelastic laminated membrane etching patterns.

Table 2   Membrane configurations

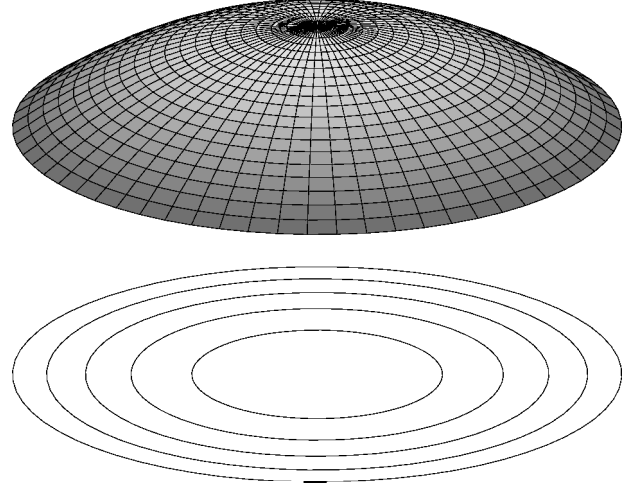| Configuration	Pattern	Area a	Area b	Area c
0	1	+	+	
1	1	0	+	
2	2	0	+	+
3	2	0	+	−
4	2	0	+	0

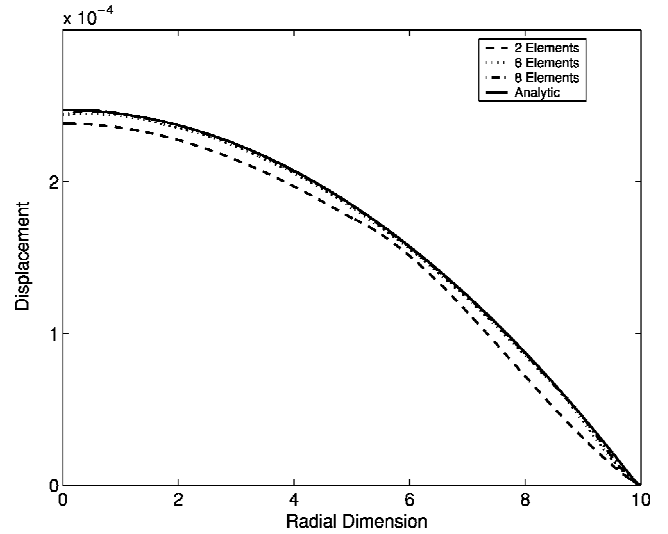Fig. 6   Configuration 0: unpressurized displacement.

Fig. 7   Configuration 0: grid density effects.

The selected grid density, as in any finite element method, plays an important role in the accuracy of the solution. Figure 7 presents the result of increasing the number of elements applied to a pressurized membrane. It is clear that increasing the number of elements improves the apparent solution, as expected. With only two elements, the model is already close to the analytical solution. Increasing the grid density provides results progressively closer to the analytical solution. It is difficult to see the difference as the grid density is increased. Figure 8 presents the boundary region effects. As the grid density increases, the model can more closely represent the curvature at the edge of the membrane.

Figure 9 shows both the advantage and disadvantage of this method. The standard deviation of the error (relative to the analytical solution) across the radial section of the solution is plotted against grid density. The method provides very good results with a very coarse grid pattern and approaches the analytical solution in an asymptotic sense. At a point, the accuracy begins to diverge from the
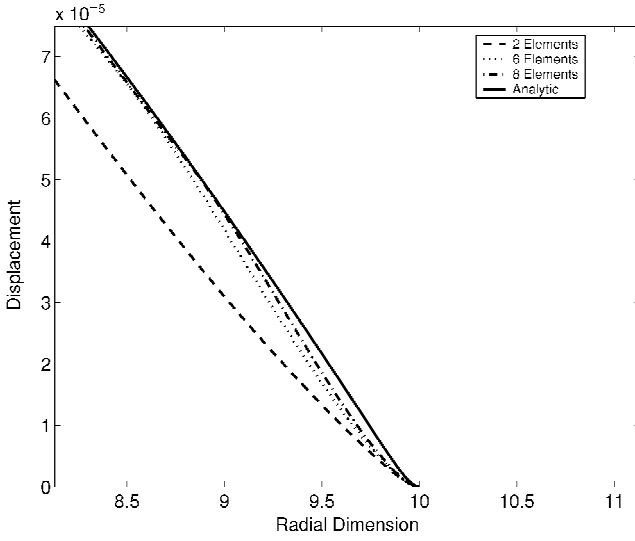
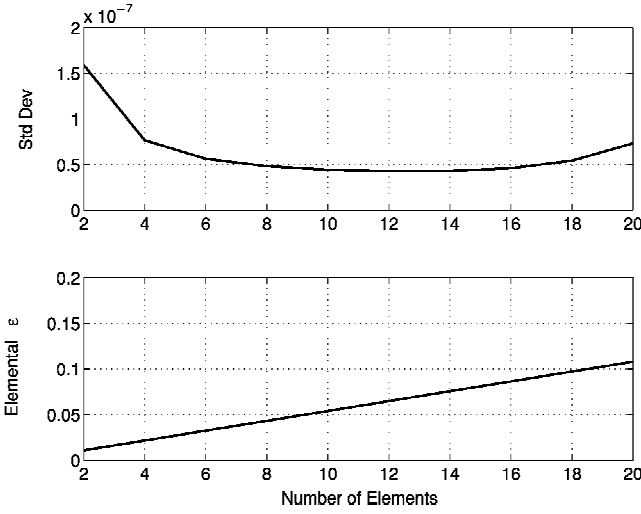Fig. 8   Configuration 0: edge grid density effects.

Fig. 9   Configuration 0: boundary-layer grid density limitations.

desired solution. The element ϵ represents the thickness-to-length ratio of the element. As the boundary region expands within the element, a point is reached where the solution method breaks down. However, the initial assumption that $\varepsilon \ll 1$ has been violated, and the method will not produce accurate results.

The effects are found to be directly proportional to the voltage applied. Regardless of pattern selected, increasing tension tends to reduce the effectiveness of the actuator. This is expected, based on previously published analytical and experimental results.[9]

Figure 10 shows the extension of this approach to discontinuous electrode coverage configurations 1–4. The surface displacements clearly indicate the localized effects. Figure 11 shows the effective difference between each configuration under a 2000-lb/in. (3.5-kN/m) tension load and applying a potential of $d_{3r} V = 10^{-8}$. The effect of pattern placement seems to have greatest effect on Zernike modes 1 and 13.

Natural Response

Figure 12 shows the effects edge tension has on the dynamic behavior of the laminate. The tension values span the expected values of such a system. Figures 12b and 12c show the effects of varying edge tension on the natural frequencies. Because the tension has a direct effect on the natural frequency, these are normalized to the fundamental mode. As the tension is increased, the frequencies approach the corresponding pure membrane modal frequencies. Figure 12b presents the normalized frequency, whereas
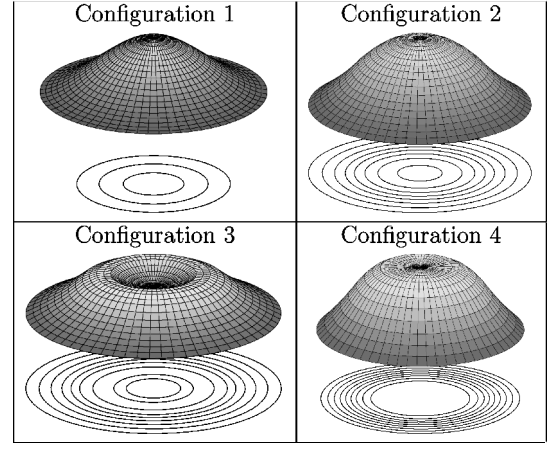
Fig. 10   Unpressurized piezoactuated displacement shapes.

Fig. 12c represents the ratio of the computed frequencies to pure circular membrane frequencies. This is expected because, as the tension gets very large, the "smallness" parameter in the analysis approaches zero. This, in effect, eliminates the platelike behavior, leaving purely membrane response. Figure 12a shows the effects of varying edge tension on the dynamic mode shapes. Notice similar results to those discussed in the preceding section. Edge tension changes will have negligible effects over the global wave front but significant effect on vibration frequency.

Forced Response

The forced response of an unpressurized membrane mirror is of particular interest. When the frequency expansion ω_i is removed, the system becomes

$$M_0 d_{2,00} + K_0 d_2 = -\hat{\Gamma}_0 \tag{55}$$

$$M_0 d_{3,00} + K_0 d_3 = -\hat{\Gamma}_1 - M_1 d_{2,00} - 2M_0 d_{2,01} - K_1 d_2 - C_1 d_{2,0} \tag{56}$$

$$M_0 d_{4,00} + K_0 d_4 = -\hat{\Gamma}_2 - 2M_1 d_{3,00} - 2M_0 d_{3,01} - M_2 d_{2,00}$$
$$- 4M_1 d_{2,01} - M_0 d_{2,11} - 2M_0 d_{2,02} - C_1 d_{3,0} - C_2 d_{2,0}$$
$$- C_1 d_{2,1} - K_1 d_3 - K_2 d_2 \tag{57}$$

where periodic excitation is applied producing

$$\hat{\Gamma}_0 = 0 \tag{58}$$

$$\hat{\Gamma}_1 = \Gamma_1 \exp[i(\Omega_k T_0 + \delta T_1)] \tag{59}$$

$$\hat{\Gamma}_2 = \Gamma_2 \exp[i(\Omega_k T_0 + \delta T_1)] \tag{60}$$

and the mass, stiffness, and damping matrices are as defined earlier. When periodic response

$$d_m = a_m \nu_m(T_1, T_2, \dots) \exp(i\Omega T_0) \tag{61}$$

is assumed, Eq. (55) represents a linear eigenvalue problem:

$$[K_0 - \lambda M_0]\nu_2 = 0 \tag{62}$$

where $\lambda = \Omega^2$. Solutions to this equation are a set of eigenvalue, mode shape pairs (λ_j, ν_{2j}) that define the first-order natural response of the system. When this result is applied to the next level [Eq. (56)], the solution can can be attained.

Inserting Eq. (61) into Eq. (56)

$$a_3[K_0 - \lambda M_0]\nu_3 \exp(i\Omega T_0) = -\Gamma_1 \exp[i(\Omega_k T_0 + \delta T_1)]$$
$$- a_2[K_1 + i\Omega_j C_1 - \lambda_j M_1]\nu_{2j} \exp(i\Omega_j T_0)$$
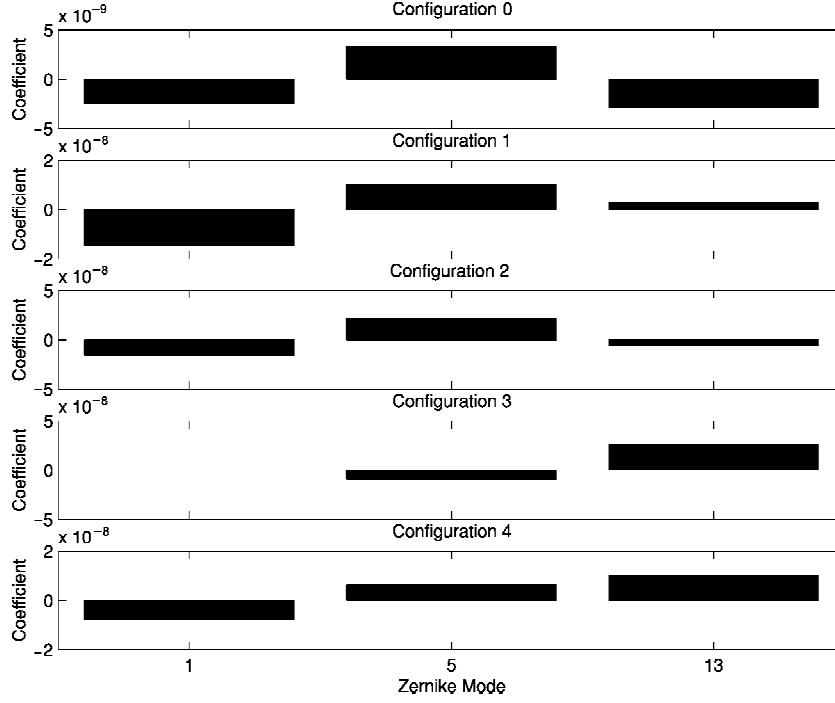$$- 2i a_2 \Omega_j M_0 \nu_{2j,1} \exp(i\Omega_j T_0) \tag{63}$$

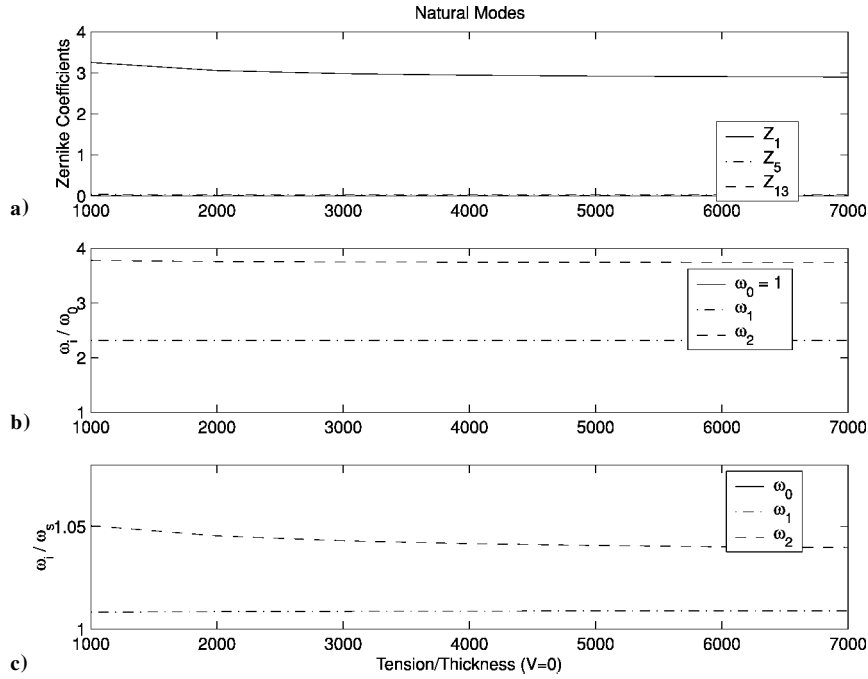**Fig. 11 Configuration Zernike coefficient comparisons.**

Fig. 12 Mode shape Zernike changes.

For this system to balance correctly, $\Omega = \Omega_j = \Omega_k$, removing all but the kth mode from the first-order solution. The resulting equation becomes

$$a_3[\boldsymbol{K}_0 - \lambda_k \boldsymbol{M}_0]\boldsymbol{\nu}_3 = -\boldsymbol{\Gamma}_1 \exp(i\delta T_1) - a_2[\boldsymbol{K}_1 + i\omega_k \boldsymbol{C}_1 - \lambda_k \boldsymbol{M}_1]\boldsymbol{\nu}_{2k}$$

$$- 2i a_2 \omega_k \boldsymbol{M}_0 \boldsymbol{\nu}_{2k,1} \qquad (64)$$

Furthermore, $\boldsymbol{\nu}_{2j}$ can only be a function of T_1 through the relationship

$$\boldsymbol{\nu}_{2k} = \hat{\boldsymbol{\nu}}_{2k}(T_2)\exp(i\delta T_1) \qquad (65)$$

for the system to balance correctly, which leaves

$$a_3[\boldsymbol{K}_0 - \lambda_k \boldsymbol{M}_0]\boldsymbol{\nu}_3 = -\boldsymbol{\Gamma}_1 - a_2[\boldsymbol{K}_1 + i\omega_k \boldsymbol{C}_1 - \lambda_k \boldsymbol{M}_1 - 2\delta\omega_k \boldsymbol{M}_0]\boldsymbol{\nu}_{2k}$$

$$(66)$$

The right-hand side must lie in the null space of the adjoint of the left-hand side. Because the left-hand side is self-adjoint, this simply means the right-hand side must be orthogonal to the solutions from Eq. (62):

$$\boldsymbol{\nu}_{2k}^T(\boldsymbol{\Gamma}_1 + a_2[\boldsymbol{K}_1 + i\omega_k \boldsymbol{C}_1 - \lambda_k \boldsymbol{M}_1 - 2\delta\omega_k \boldsymbol{M}_0]\boldsymbol{\nu}_{2k}) = 0 \qquad (67)$$
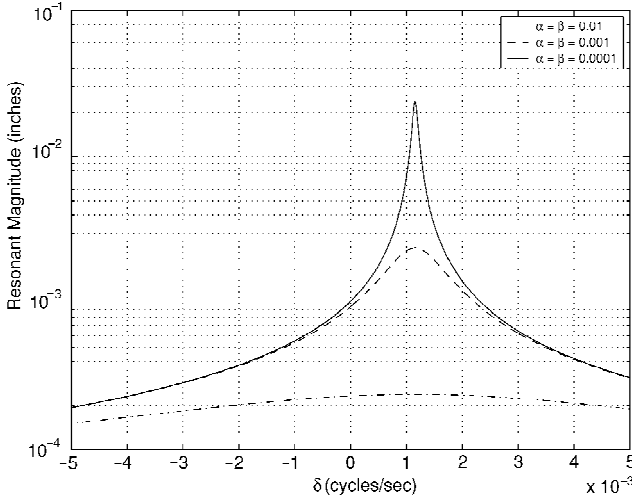
Fig. 13 Membrane forced response (damping effects).

The only unknown here is the amplitude of the first-order response:

$$a_2 = \frac{-\boldsymbol{\nu}_{2k}^T \boldsymbol{\Gamma}_1}{\boldsymbol{\nu}_{2k}^T [\boldsymbol{K}_1 + i\omega_k \boldsymbol{C}_1 - \lambda_k \boldsymbol{M}_1 - 2\delta\omega_k \boldsymbol{M}_0]\boldsymbol{\nu}_{2k}} \qquad (68)$$

When this value is applied back into Eq. (66), the right-hand side now resides only in the space remaining after removal of $\boldsymbol{\nu}_{2k}$. Because the left-hand side of Eq. (66), with λ_k, spans all but the space of $\boldsymbol{\nu}_{2k}$, there is a unique solution. This equation becomes

$$a_3 [\boldsymbol{K}_0 - \lambda_k \boldsymbol{M}_0]\boldsymbol{\nu}_3 = \boldsymbol{B}_1 \qquad (69)$$

where $\boldsymbol{B}_1$ is the constant vector resulting from the insertion of the known a_2 into Eq. (66). Solving for the a_3 terms produces the contributory responses of each mode other than ω_k. When this method is used, the forced response can be approximated.

When this is applied to the earlier described unpressurized membrane, Fig. 13 shows an effective shift of the first mode, regardless of damping. The damping values were chosen to illustrate the effect, not imply actual known values.

Additionally, it is clear significantly higher deflections are possible dynamically than statically. This could imply a piezopolymer laminate with limited effect for static shape corrections due to the local effects it produces dynamically can provide a significant response. This indicates a laminate design may enable active vibration control over the large surface area of the reflector.

Conclusions

This paper presented the application of the MIMS to axisymmetric laminated piezothermoelastic plate membranes. MIMS was applied through a finite element methodology producing results for systems more complicated than the analytical method can support. The analytical solution was presented illustrating the limitations of such methods. Although some discontinuity was modeled in the form of through-the-thickness laminate properties, the system must be layerwise continuous, not allowing uneven electrode coverage. The MIMS finite element solution of the axisymmetric circular membrane was developed, which allowed partial electrode coverage. The partial coverage allows design flexibility to tailor the distribution as desired.

The results indicate a laminate of piezoelectric polymer material adhered to the nonreflective surface of an inflatable optical reflector can have a significant effect on the wave front being measured. Several wavelengths of actuation are possible, providing a small amount of shape control. The areas of electrode coverage can be designed to provide the desired controllability. Additionally, this laminate also appears to be a good candidate for active vibration suppression of these materials.

The MIMS methodology, when applied through a finite element approach, appears to show promise for systems that exhibit localized behavior such as boundary regions. When this procedure was used, the boundary region effects were captured without the need for large grid densities. When the MIMS methodology is used, a more efficient modeling capability might be created allowing more complex analysis in a significantly reduced time period.

Appendix: Optical Modes

Optical membrane reflectors are often analyzed from a purely structural point of view. From a systems view, the structural response is important, but only to the extent that it impacts the overall mission. An optical reflector, whether a thin membrane or a glass mirror, is only as good as the wave front produced. Mechanical analysis of a circular membrane includes the dynamic vibration modes, whereas an optical analysis would include the wave front aberrations.

A common mathematical wave front definition using a series of orthogonal Zernike functions is presented. A section is also included that presents a method to map structural shapes to these Zernike functions. A direct mapping is only available for continuous functions. When intermediate functions, based on Zernike functions, are used, the mapping can be accomplished.

Optical Modes

Circular wave fronts are often represented by different families of orthogonal functions. As an example, Zernike functions are commonly used.[10] This family allows the wave front distortion to be defined as

$$w(r, \theta) = \sum_{n=0}^{k} \sum_{m=0}^{n} A_{mn} U_{mn}(r, \theta) = \sum_{h=0}^{y} A_h U_h(r, \theta) \qquad (A1)$$

The relationship between h and n, m can be represented by

$$h = [n(n+1)/2] + m + 1 \qquad (A2)$$

which is not a unique mapping, but is used here. The Zernike functions U_{mn} are

$$U_{mn}(r, \theta) = \begin{matrix} R_{mn}(r)\sin(n-2m)\theta, & n-2m > 0 \\ R_{mn}(r)\cos(n-2m)\theta, & n-2m < 0 \end{matrix} \qquad (A3)$$

where

$$R_{mn}(r) = \sum_{s=0}^{m} (-1)^s \frac{(n-s)!}{s!(m-s)!(n-m-s)!} r^{(n-2s)} \qquad (A4)$$

Note that only positive powers of r are retained, that is, only values of s that result in positive $n-2s$ are included in the summation.

These modes are orthogonal through the relationship

$$\int_0^{2\pi} \int_0^1 U_{mj}(r, \theta) U_{mk}(r, \theta) r \, dr \, d\theta = \frac{\pi}{2(n+1)} \delta_{jk} \qquad (A5)$$

over the unit circle, where δ_{jk} is the Kronecker delta.

Figure A1 shows the Zernike functions for given m and n values. The upper three-dimensional plot in each cell represents an actual planar wave front if an aberration of the corresponding Zernike function exists. Under each plot is a contour plot of the surface indicating the type of pattern such a wave front would produce in an interferometer. When the extremely small displacements relative to the area of concern are recognized, the wave front distortion can be estimated to be twice the surface displacement. A mapping between surface shape and Zernike functions can easily be created through application of orthogonality principles.
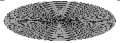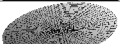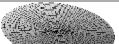
$n \downarrow \ m \rightarrow$	0	1	2	3	4
0	Z_1				
1	Z_2	Z_3			
2	Z_4	Z_5	Z_6		
3	Z_7	Z_8	Z_9	Z_{10}	
4	Z_{11}	Z_{12}	Z_{13}	Z_{14}	Z_{15}

Fig. A1   Zernike modes.

Defining Wave Front Aberrations Using Zernike Functions

Determination of the least-squares, best-fit Zernike coefficients that represent a circular wave front requires the use of intermediate orthonormal functions. The remainder of this section is modified from Malacara et al.[10] for use in this analysis.

Given N measured points with coordinates (r_n, θ_n) and corresponding wave front displacements W'_n, the discrete variance $\bar{v}^2$ from a closed analytical function $W(r, \theta)$ can be defined as

$$\bar{v}^2 = \frac{1}{N} \sum_{n=1}^{N} [W'_n - W(r_n, \theta_n)]^2 \qquad (A6)$$

In the case considered here, the analytic function can be represented as a linear combination of intermediate orthonormal functions $\bar{V}_h(r, \theta)$, to be defined later:

$$W(r_n, \theta_n) = \sum_{h=1}^{L} B_h \bar{V}_h(r_n, \theta_n) \qquad (A7)$$

The least-squares, best-fit is then calculated by minimizing the variation

$$\frac{\partial \bar{v}}{\partial B_p} = 0 \qquad (A8)$$

where $p = 1, 2, \ldots, L$, which produces

$$\sum_{h=1}^{L} B_h \sum_{n=1}^{N} \bar{V}_h(r_n, \theta_n) \bar{V}_p(r_n, \theta_n) = \sum_{n=1}^{N} W'_n \bar{V}_p(r_n, \theta_n) = 0 \quad (A9)$$

which requires $\bar{V}_h$ to satisfy the following orthonormality condition:

$$\frac{\sum_{n=1}^{N} \bar{V}_h(r_n, \theta_n) \bar{V}_p(r_n, \theta_n)}{\sum_{n=1}^{N} \bar{V}_p^2(r_n, \theta_n)} = \delta_{hp} \qquad (A10)$$

where δ_{hp} is the Kronecker delta. The coefficients B_h are

$$B_h = \frac{\sum_{n=1}^{N} W'_n \bar{V}_p(r_n, \theta_n)}{\sum_{n=1}^{N} \bar{V}_p^2(r_n, \theta_n)} \qquad (A11)$$

Using Gram–Schmidt orthogonalization, the orthonormal functions $\bar{V}_r$ can be described using the following relationship:

$$\bar{V}_h(r, \theta) = U_h(r, \theta) + \sum_{s=1}^{h-1} D_{hs} \bar{V}_s(r, \theta) \qquad (A12)$$

where $h = 1, 2, \ldots, y$ and $U_r(r, \theta)$ are the Zernike functions [Eq. (A3)]. Using the ortho-normality condition [Eq. (A10)], we can derive the coefficients D_{hs} as

$$D_{hs} = -\frac{\sum_{n=1}^{N} U_h(r_n, \theta_n) \bar{V}_p(r_n, \theta_n)}{\sum_{n=1}^{N} \bar{V}_p^2(r_n, \theta_n)} \qquad (A13)$$

where $h = 2, 3, \ldots, y$ and $p = 1, 2, \ldots, h - 1$.

Finally, substituting Eq. (A10) into Eq. (A7) gives the following best-fit decomposition of the wave front $W(r, \theta)$ in terms of a corresponding linear combination of Zernike functions:

$$W(r, \theta) = \sum_{h=1}^{L} A_h U_h(r, \theta) \qquad (A14)$$

where

$$A_h = B_h + A_q D_{qs} \qquad (A15)$$

and $h = 1, 2, \ldots, y$, $q = h + 1$, and $A_z = 0 \ \forall z < 0$. Based on this procedure, Zernike coefficients can be computed for arbitrary wave front aberrations.

References

[1]Carreras, R., Wilkes, J., Marker, D., Duneman, D., and Rotgé, J., "Deployable Near-Net Shape Membrane Optics," *High Resolution Wavefront Control: Methods, Devices, and Applications*, Vol. SPIE 3760, Society of Photo-Optical Instrumentation Engineers, Bellingham, WA, 1999, pp. 232–238.

[2]Greschik, G., Mikulas, M., and Palisoc, A., "Approximations and Errors in Pressurized Axisymmetric Membrane Shape Predictions," AIAA, Reston, VA, 1998, pp. 2761–2771.

[3]Rogers, J., "Modelling Axisymmetric Optical Precision Piezoelectric Membranes," Ph.D. Dissertation, Aeronautical and Astronautical Engineering Dept., Air Force Inst. of Technology, Wright–Patterson AFB, OH, Oct. 2001.

[4]Rogers, J., and Agnes, G., "Formulation of Asymptotic Finite Elements Using the Method of Integral Multiple Scales," AIAA Paper 2002-1663, April 2002.

[5]Rogers, J. W., Jr., and Agnes, G. S., "Asymptotic Finite Elements Introducing the Method of Integral Multiple Scales," *AIAA Journal* (to be published).

[6]Cook, R., Malkus, D., and Plesha, M., *Concepts and Applications of Finite Element Analysis*, 3rd ed., Wiley, New York, 1974, pp. 75–78.

[7]Saada, A., *Elasticity Theory and Applications*, 2nd ed., Krieger, Malabar, FL, 1993, p. 138.

[8]Rogers, J., and Agnes, G., "Modeling a Piezoelectric Laminated Plate-Membrane," *Journal of Intelligent Material Systems and Structures*, Vol. 6, No. 10, 2002.

[9]Greschik, G., Palisoc, A., Cassapakis, C., Veal, G., and Mikulas, M., "Sensitivity Study of Precision Pressurized Membrane Reflector Deformations," *AIAA Journal*, Vol. 39, No. 2, 2001, pp. 308–314.

[10]Malacara, D., Servín, M., Malacara, Z., *Interferogram Analysis for Optical Testing*, Marcel Dekker, New York, 1998, pp. 98–103.

M. S. Lake
Associate Editor